



HAL
open science

3D laser engineering of molten core optical fibers: toward a new generation of harsh environment sensing devices

Yitao Wang, Maxime Cavillon, John Ballato, Thomas Hawkins, Tino Elsmann, Manfred Rothhardt, Rudy Desmarchelier, Guillaume Laffont, Bertrand Poumellec, Matthieu Lancry

► To cite this version:

Yitao Wang, Maxime Cavillon, John Ballato, Thomas Hawkins, Tino Elsmann, et al.. 3D laser engineering of molten core optical fibers: toward a new generation of harsh environment sensing devices. *Advanced Optical Materials*, 2022, 10 (18), pp.2200379. 10.1002/adom.202200379 . hal-04125496

HAL Id: hal-04125496

<https://hal.science/hal-04125496>

Submitted on 12 Jun 2023

HAL is a multi-disciplinary open access archive for the deposit and dissemination of scientific research documents, whether they are published or not. The documents may come from teaching and research institutions in France or abroad, or from public or private research centers.

L'archive ouverte pluridisciplinaire **HAL**, est destinée au dépôt et à la diffusion de documents scientifiques de niveau recherche, publiés ou non, émanant des établissements d'enseignement et de recherche français ou étrangers, des laboratoires publics ou privés.



Distributed under a Creative Commons Attribution - NonCommercial 4.0 International License

3D Laser Engineering of Molten Core Optical Fibers: Toward a New Generation of Harsh Environment Sensing Devices

Yitao Wang, Maxime Cavillon, John Ballato, Thomas Hawkins, Tino Elsmann, Manfred Rothhardt, Rudy Desmarchelier, Guillaume Laffont, Bertrand Poumellec, and Matthieu Lancry*

Aluminosilicate glasses offer wide-ranging potential as enabling materials for a new generation of optical devices operating in harsh environments. In this work, a nonconventional manufacturing process, the molten core method, is employed to fabricate and study sapphire (Al_2O_3) and YAG (yttrium aluminum garnet) derived all-glass silicate optical fibers in which a femtosecond (fs) laser is used to imprint oriented nanostructures inside the fiber cores. Both writing kinetics and thermal stability of the laser-modified regions are investigated over a wide temperature range (20–1200 °C). The laser-imprinted modifications in these high alumina-content fibers exhibit improved thermal stability with respect to commercial pure silica and GeO_2 -doped silica analogs. Furthermore, optical devices in the form of Rayleigh backscattering and fiber Bragg grating sensors are fabricated to demonstrate the high-temperature sensitivity and stability of these nonconventional fibers. This functionalization of aluminosilicate fibers by fs-laser direct writing opens the door to a new generation of optical devices suitable for high-temperature operation.

(kW fiber lasers, long-term optical data storage such as Microsoft's "project silica",^[1] etc.) and optical sensing (structural health monitoring of engines, deep drilling).^[2] In most applications operating in a HT environment, refractory crystalline oxide materials such as alumina (Al_2O_3) or zirconia (ZrO_2) are candidates of choice, due to their high melting points and good resistance to oxidation and abrasion. Furthermore, directionally solidified eutectic ceramics (e.g., unidirectionally solidified Al_2O_3 /oxide eutectic composite made of perovskite or garnet phase) also can improve thermal stability,^[3] as demonstrated for instance in aircraft gas turbines and thermal power generation systems (e.g., operation for 1000 h at 1700 °C).

However, other HT applications, such as long-lived data storage for the zetta-byte era^[1] or optical sensors (down-hole oil/gas exploration, monitoring of structure health, temperature regulation of engines, etc.) require using glass materials that can be functionalized and shaped into chips, disks, planar waveguides or optical fibers. Both the materials and geometric designs need be considered due to practical demands, such as compactness and lightness, flexibility, high-transparency, fast and complex manufacturing shaping, chemical/radioactive/electromagnetic resistance, and low cost. For these reasons,

1. Introduction

There is an increasingly broad demand for high-temperature (HT) materials for a wide range of industrial applications, including in aviation/space (aeronautical turbine engine, space launcher), manufacturing (3D laser additive manufacturing of metal or ceramics parts, steel industry), nuclear (instrumentation of future reactors and tokamaks), or again in photonics

Y. Wang, M. Cavillon, B. Poumellec, M. Lancry
Institut de Chimie Moléculaire et des Matériaux d'Orsay
(ICMMO/SP2M/MAP)
Université Paris-Saclay
CNRS
Orsay Cedex 91405, France
E-mail: matthieu.lancry@u-psud.fr

 The ORCID identification number(s) for the author(s) of this article can be found under <https://doi.org/10.1002/adom.202200379>.

© 2022 The Authors. Advanced Optical Materials published by Wiley-VCH GmbH. This is an open access article under the terms of the Creative Commons Attribution-NonCommercial License, which permits use, distribution and reproduction in any medium, provided the original work is properly cited and is not used for commercial purposes.

J. Ballato, T. Hawkins
Center of Optical Materials Science and Engineering Technologies (COMSET)
Department of Materials Science and Engineering
Clemson University
Clemson, South Carolina, USA
T. Elsmann, M. Rothhardt
Leibniz Institute of Photonic Technology
Albert-Einstein-Str. 9, 07745 Jena, Germany
R. Desmarchelier, G. Laffont
Université Paris Saclay
CEA, List
Palaiseau F-91120, France

DOI: 10.1002/adom.202200379

glass optical materials have been extensively used and further functionalized over the past three decades.^[4]

Concomitant advances in materials chemistry, glass manufacturing methods, and ultrafast laser nanostructuring of transparent materials (i.e., to functionalize the material), open the door to develop optical devices that can withstand harsh environments,^[2b,4b] such as thermo-mechanical loads much beyond the 800 °C limit or kW power propagation. Thus, developing a new generation of reliable and robust sensing technologies for industrial processes that take place under extreme physical conditions requires improved thermal stability of related optical devices.^[5] The bottleneck to this continuous enhancement of HT stability is related to the intrinsic nature of glass and the laser-induced structural changes that enable the desired performance of the optical device. This includes considering HT dynamics of viscous flow, chemical migration, and stress relaxation.^[6]

To date, most practical optical fibers are made using chemical vapor deposition (CVD) techniques and are generally limited to very high SiO₂ concentrations with only a few selected dopants. To go beyond the compositional limitations imposed by conventional CVD techniques,^[7] this work investigates lower silica content optical fibers fabricated using a nonconventional (i.e., as opposed to CVD) approach to novel optical fibers, the molten core method (MCM).^[8] The MCM permits large compositional flexibility in the fiber core, and the realization of fibers with “unstable” core compositions, such as those studied here derived from crystalline hosts such as sapphire (Al₂O₃), YAG (yttrium aluminum garnet), or ZrO₂. Complementing these nonconventional materials is fs laser direct writing (FLDW) as a nonconventional tool to functionalize the glass by restructuring the local molecular order to enable the imprinting of permanent modifications of optical properties. Aspects to this light-matter interaction are fundamentally new, e.g., electronic plasma coexisting inside a solid for a fraction of picoseconds, and subsequent material restructuring shaped by intense light fields. The underlying processes occur in highly excited and far-from-equilibrium states, yielding 3D writing of oriented structural modifications such as self-organized nanostructures (so-called nanogratings,^[9] also denoted “Type II”), directionally solidified oxide decomposition,^[10] or oriented nanocrystals^[11] with outstanding thermal stability.^[12]

In this paper, inspired by unidirectionally solidified Al₂O₃-based eutectics,^[3] fs-laser writing into sapphire-derived and YAG-derived all glass optical fibers is investigated (all fiber cores are amorphous). The two aluminosilicate core fibers possessed very high alumina concentrations: 51.5%Al₂O₃ – 48.5%SiO₂^[13] and 42.5%Al₂O₃ – 57.5%SiO₂,^[14] respectively, while the YAG-derived glass fiber has a slightly higher silica content but was still highly modified by conventional optical fiber standards with a composition of 71.8%SiO₂ – 19.5%Al₂O₃ – 8.7%Y₂O₃.^[15]

The properties and performance of these fibers are compared to those of standard single-mode fiber (SMF-28, Corning). FLDW was performed to imprint an oriented phase separation taking the form of nanogratings, and thermal stability of the aforementioned modifications was thus studied through isochronal annealing experiments. The approach was then validated through fabrication of optical frequency-domain reflectometry (OFDR) based sensors (Rayleigh backscattering) and fiber Bragg gratings.

2. Results and Discussion

2.1. Writing Kinetics of Type-II Modifications in Sapphire- and YAG- Derived Optical Fibers

Measurements of retardance, *R*, as a function of the laser pulse energy are displayed in **Figure 1** for all investigated fibers. The data on pure silica (F300 Suprasil) and conventional single-mode fiber (SMF-28) are also shown for comparison. The lowest energy at which a nonzero *R* value is detected corresponds to the IR-fs-Type II threshold. This is where polarization-dependent anisotropic optical properties begin to appear in the irradiated lines indicating the formation of nanogratings as further confirmed by scanning electron microscopy (SEM, see next section).

As described in the Experimental Section, a strong linear birefringence can be detected by polarized optical microscopy between crossed polarizers when the energy exceeds the Type II threshold. This likely originates from the formation of nanogratings^[16] as it is well known in silica or slightly doped silica glasses.^[17] In the experimental conditions, the Type II thresholds are located in the range of 0.3–0.4 μJ and are compositionally dependent.^[17a] Here, the threshold value slightly depends on the Al₂O₃ concentration and increased to (0.44 ± 0.05) μJ for both aluminosilicate fibers. In contrast, other fibers exhibit very similar behavior with threshold values of ≈0.35 μJ. Above the Type II threshold, the retardance generally follows a monotonic increase with the pulse energy with *R* rapidly reaching a plateau of about *E*_p = 0.75 μJ for all glass compositions. As observed in Figure 1, the pure silica cladding and the SMF-28 fiber (96 mol% silica) display a similar trend with the low pulse energy (<1 μJ). Interestingly, the two aluminosilicate fibers exhibit lower retardance values relative to the silica-rich glasses. The *R* values for the aluminosilicate fibers are approximately half the values of pure silica (50 and 100 nm at *E*_p = 1.5 μJ, respectively); however, this is sufficient for most of the targeted applications.

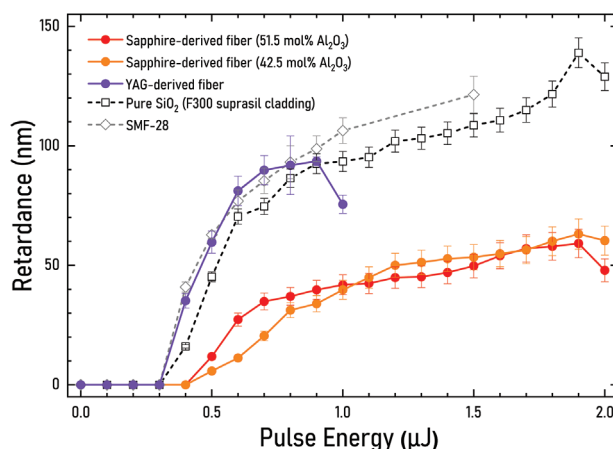


Figure 1. Retardance (*R*) as a function of pulse energy for sapphire-derived fibers (red and orange), pure silica (black), YAG-derived fiber (purple), and a SMF-28 fiber (grey). Experimental conditions are: $\lambda = 1030$ nm, 100 kHz, 100 $\mu\text{m s}^{-1}$, 1000 pulses μm^{-1} , NA = 0.6, pulse duration = 250 fs, laser polarization parallel to the writing direction.

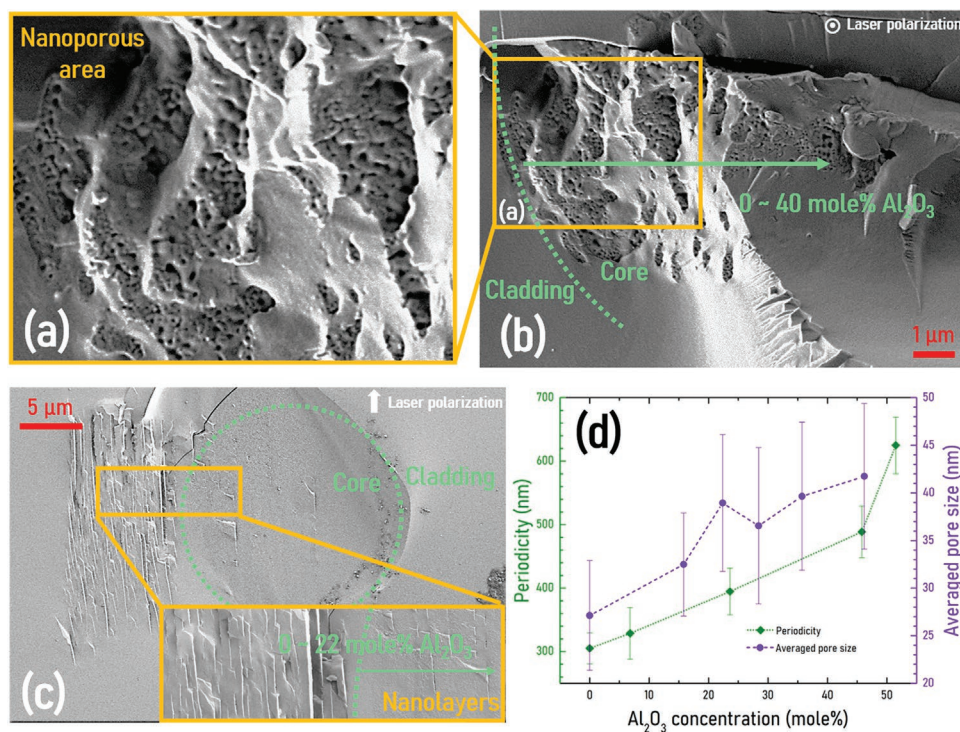


Figure 2. Scanning electron micrographs of sapphire-derived fiber, for a,b) parallel, and c) perpendicular laser polarization direction with respect to the writing direction. Experimental conditions are: $\lambda = 1030$ nm, 100 kHz, $100 \mu\text{m s}^{-1}$, $1000 \text{ pulses } \mu\text{m}^{-1}$, $\text{NA} = 0.6$, $E = 1.0 \mu\text{J}$ per pulse. d) averaged nanopore size and periodicity of nanoporous planes as a function of the Al_2O_3 content in the fiber core, results are measured from (a)-(b)-(c).

2.2. Scanning Electron Micrographs of the Aluminosilicate Fibers

To investigate the observed differences and trends in retardance values, and to understand the effect of high Al_2O_3 concentrations on the final morphology of the modified regions, scanning electron microscopy (SEM) was performed. The latter confirmed the existence of nanogratings in both cores and cladding of both sapphire- and YAG-derived all-glass fibers. These nanogratings are at the root of the measured birefringence, which is related to the refractive index contrast along these nanogratings. This is exemplified in **Figure 2**, where SEM micrographs of the sapphire-derived fiber cross-sections are selected and reported, using both the laser polarization direction oriented perpendicular (Figure 2a,b) and parallel (Figure 2c) to the laser writing direction.

As found in Figure 2c, upon moving from the core/cladding interface to the core center, a periodic structure composed of nanolayers can be easily observed. Similarly, in Figure 2a,b, using a polarization orientation parallel to the writing direction, the formation of nanoporous structure is clearly identified throughout the compositional range. Figure 2d summarizes the evolution of the average pore size and periodicity in the nanoporous area and as a function of Al_2O_3 concentration. Hence as one moves from the cladding and into the core, the averaged spacing (periodicity) gradually increases with an increase in Al_2O_3 concentration. In the silica cladding the measured value is 305 ± 40 nm, which is quite similar to the values reported previously.^[15] When the Al_2O_3 concentration is maximized

(51.5%) the average spacing more than doubles to 630 ± 40 nm. The larger period for higher Al_2O_3 content is attributed to both the larger refractive index but also to the higher Type II threshold.^[18] It is also worth noting that the average nanopore diameter follows the same trend since it increases by around 50%, i.e., from 27 ± 5 nm in the fiber cladding up to 42 ± 7 nm near the core center.

For completeness, the existence of nanogratings can still be observed up to the core center in agreement with recent work on bulk samples.^[18] All these results suggest that the measured retardance in aluminosilicate fibers has the same origin as for SiO_2 , i.e., production of a periodic array of porous nanoplanes separated by nonporous glass,^[10] mostly resulting in a form birefringence.^[19]

2.3. Thermal Stability of Type II Modification in Aluminosilicate Fibers

Step isochronal annealing ($\Delta t = 30$ min) was carried out in order to investigate the thermal stability of Type II modifications in the sapphire-derived fiber. The fiber was irradiated at increasing pulse energies in order to study the dependence of the thermal stability with the laser writing conditions. **Figure 3** shows the evolution of normalized retardance, $R_{\text{norm}}(\Delta t, T)$, as a function of the annealing temperature (T).

Several features in the normalized retardance $R_{\text{norm}}(\Delta t, T)$ can be distinguished according to the annealing temperature and depending on the pulse energy considered.

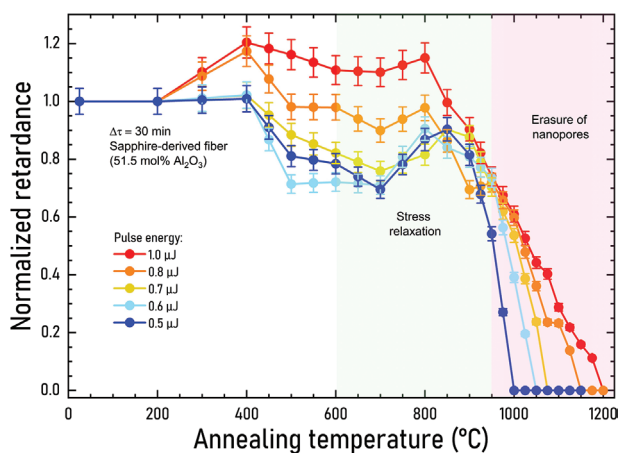


Figure 3. Normalized retardance $R_{\text{norm}}(\Delta t, T)$ as a function of annealing temperature for a sapphire-derived fiber irradiated with different pulse energies. Experimental conditions are: $\lambda = 1030$ nm, 100 kHz, $100 \mu\text{m s}^{-1}$, 1000 pulses μm^{-1} , NA = 0.6, laser polarization perpendicular to the writing direction. All measurements were performed at room temperature.

Within the Type II regime and for pulse energy less than $0.7 \mu\text{J}$, the retardance exhibits a monotonic decrease immediately after the heat treatment from 400 to 700 °C. Depending on the pulse energy, the largest decay of R_{norm} was about 35% for the lowest writing pulse energy ($E = 0.5 \mu\text{J}$). Then there is a slight “recovery,” namely an increase of the measured $R_{\text{norm}}(\Delta t, T)$ within the 600–800 °C temperature range, and which appears around $0.9T_g$ (T_g is the glass transition temperature), typical of stress relaxation in glass.^[20] This agrees well with the T_g value of 50% Al_2O_3 – 50% SiO_2 that is estimated to be around 830–850 °C.^[21]

For pulse energy greater than $0.7 \mu\text{J}$, the $R_{\text{norm}}(\Delta t, T)$ exhibits a different thermal behavior. It increases from the beginning of the heat treatments at 200 °C up to 400 °C. Then, R_{norm} “fluctuates” between 400 and 800 °C. However, for the line written at $1 \mu\text{J}$, an R_{norm} increase by about 15%–20% was observed compared with its initial value. This is in agreement with the results related to Type II fiber Bragg gratings reported in aluminosilicate fibers with Al_2O_3 content up to 30 mol% and in silica fibers.^[22] Then, as the annealing temperature increases, $R_{\text{norm}}(\Delta t, T)$ starts to diminish dramatically at 800–950 °C. At first all curves exhibit a steep decay of about 30%–35% after the heat-treatment ≈ 850 °C–950 °C. Following that, the complete erasure is then observed from 1000 to 1200 °C and no measurable birefringence can be found after 30 min at 1200 °C. The final decay is attributed to the erasure of the nanoporous layers as was recently modeled based on Rayleigh–Plesset effects.^[23] In addition, it is expected that the higher the laser pulse energy, the higher the annealing temperature required to completely erase this last contribution.

2.4. Discussion Around the Erasure Mechanisms

To interpret the different erasure kinetics, it must be mentioned that the total measured retardance can be composed of additive/subtractive contributions, which are not independent

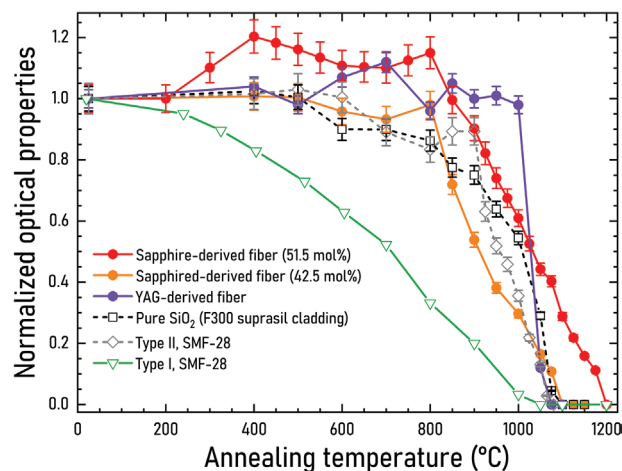


Figure 4. The normalized retardance $R_{\text{norm}}(\Delta t, T)$ as a function of temperature for two sapphire-derived fibers (red and orange), a SMF-28 and pure SiO_2 (grey and black). Data from a YAG-derived fiber (purple),^[15] and the Type I modifications in SMF-28 (green) are also shown for sake of comparison. “Optical properties” correspond to normalized retardance values for all data set excepted for Type I, SMF-28 (refractive index variation). Experimental conditions are: Pulse energy = $1 \mu\text{J}$, $\lambda = 1030$ nm, 100 kHz, $100 \mu\text{m s}^{-1}$, 10^3 pulses μm^{-1} , NA = 0.6, laser polarization perpendicular to the writing direction.

(e.g., stress is related to the permanent volume changes) of each other. Recently, the various trends observed in $R_{\text{norm}}(\Delta t, T)$ evolution, in relationship with different erasure mechanisms, has been investigated in great details in silica.^[16] These contributions are divided into three categories:

- i) First the birefringence of the so called “Type I”-like modification can be considered as a refractive index modification arising from a combination of defects, densification, and associated stress-induced birefringence. Point defect centers are bleached under fairly low-temperature thermal treatment (< 600 °C).^[16] and there is only a minor (or negligible) effect on the measured retardance within this temperature range.^[24] The relative stability of average refractive index changes related to Type I modifications is shown in **Figure 4**.
- ii) Then Type II modifications yield to the presence of a stress field taking its roots from two separated origins. The former is from Type I and disappears along with it below T_g . The second one comes from nanoporous layers and will relax plastically (a plastic deformation around nanopores occurs) because nanopores are more stable and will ultimately erase at higher temperatures. The subsequent rise from 600 to 950 °C (Figure 3) is attributed to the co-existence of “Type I like” modifications (i.e., mostly densification and related tensile stress) with the ones specific of Type II, i.e., nanogratings structuration with porous nanolayers. The progressive erasure of the former occurred at this stage and eventually causes an “abnormal” increase of the retardance R (as observed here but also in the literature (Prof. Kazansky’s group in bulk glass and Prof. Mihailov’s group in fibers^[12]). Upon annealing, a part of the stress is expected to relax when the temperature approaches $0.9T_g$ for a few tens of minutes. Here this stress relaxation starts from 800 °C, which

correlates with the “1st component” decay of $R_{\text{norm}}(\Delta t, T)$ in the 800–950 °C range observed in Figures 3 and 4. Noted here is that the compressive stress field produced by the nanoporous layers does not disappear with the annihilation of the nanopores themselves (which takes place at a higher temperature) but rather by plastic deformation of the glass around the nanopores as extensively discussed in our previous papers in bulk silica glass.^[23]

- iii) The third contribution is the form birefringence related to the nanoporous arrangement within the nanolayers. More details can be found in Ref. [23] and leads to the conclusion that the porosity plays a key role in the erasure of nanogratings and their associated birefringence in a high-temperature regime. In particular, the Rayleigh–Plesset simulation sheds light on the major role played by the viscous behavior of the glass, at high temperature, that is the major parameter that drives the nanogratings erasure and related form birefringence.
- iv) The higher the laser pulse energy, the higher the full erasure temperature. This can be explained as follow: as the energy increases so too does the deposited dose. This is a typical case described in Ref. [25] where there is a link between writing and erasure. Consequently, as a higher energy is used in the laser writing process, the demarcation energy increases, and more stable species or larger size nanopores are produced.^[23] The subsequent modifications become increasingly stable. The process is reflective of the distribution of energies possible within amorphous materials, i.e., distribution of local structures or atomic configurations.

2.5. Comparing the Overall Thermal Performance of the Optical Fibers and devices

Accelerated aging experiments are performed on the sapphire-derived fibers, as well as on a SMF-28 fiber and Suprasil F300 pure silica glass. All samples were exposed to similar experimental conditions. Figure 4 displays an aggregate of the normalized retardance $R_{\text{norm}}(\Delta t, T)$ as a function of temperature. Note that here, annealing of samples written with fs laser pulse energy was performed at 1.0 μJ, which corresponds to the stable range of Type II modifications for each sample (in term of writing kinetics) and can facilitate reliable measurements of the retardance. The normalized refractive index variation corresponding to Type I modifications in SMF-28 (green) is also shown for sake of comparison.

For the Type II irradiated region, the $R_{\text{norm}}(\Delta t, T)$ value starts to decrease slowly for temperatures higher than 800 °C. The changes in Si–O three and four-member rings anneal out in the 700–900 °C range, and are well correlated with the structural relaxation of densified silica formed within the nanograting regime.^[25] Then as the annealing temperature is increased, stress relaxes, and consequently to this the stress-induced birefringence further lessens. Finally, the erasure of nanopores (at the root of the refractive index contrast along nanogratings) leads to a very steep decrease of the form birefringence induced by themselves, and the R_{norm} value drops to zero in the range of 1075–1200 °C depends on the chemical composition of the fibers. By comparing thermal behavior for

both SMF-28 fiber and YAG-derived fiber, the former exhibits a decrease in R values starting roughly \approx 900 °C and fully disappearing at 1080 °C. On the other hand, the latter YAG-derived fiber demonstrates a better thermal stability (defined as the T at which the curve falls down below $R_{\text{norm}} = 1$) between 800 and 1000 °C when compared with the other fibers. However, its R_{norm} diminishes dramatically above 1000 °C.

Conversely, the fs-induced modifications in the high Al_2O_3 containing aluminosilicate fibers own the highest thermal stability since exploitable optical properties (here the retardance) survived at higher temperatures (typically until 1175 °C). This performs even better than pure silica glass and thus all-silica microstructured optical fibers. Previous work suggests that the formation of nanogratings in aluminosilicate glasses could be due to the separation of Al_2O_3 -rich phase in a SiO_2 -rich matrix.^[18] The nanogratings thermal stability could also be related to phase immiscibility.^[26] As shown in Figure 4, the most Al_2O_3 -containing sapphire-derived fiber (51.5 mol% Al_2O_3) performs better than the other sample (42.5 mol% Al_2O_3) during identical annealing, which could be attributed to the increase in aluminum coordination (four, five, sixfold coordination^[27]), along with an associated increase of both glass network cross-linking density and bond strength.

2.6. Fabrication of High-Temperature Sensors

To demonstrate the ability of molten core fibers to be used for imprinting sensing devices, distributed sensors based on Rayleigh backscattering are fabricated in sapphire-derived, YAG-derived, and SMF-28 fiber segments, a first to the Authors knowledge. The Rayleigh backscattered signal, working on the principle of OFDR, was monitored during the step isochronal annealing process, and the results are reported in Figure 5. Additionally, for the SMF-28, the results were compared with retardance $R_{\text{norm}}(\Delta t, T)$ evolution obtained by simulation using the Rayleigh–Plesset equation (simulation conditions: surface energy $S = 0.3 \text{ J m}^{-2}$; pore size diameter = 15 nm).^[23] As illustrated in the inset of Figure 5a, the scattered light originating from the presence of fs-laser modifications is re-captured by the waveguide and sent backward to the light collector. This backward propagating Rayleigh scattered light has a time delay that can be used for distributed sensing.^[28] Using an OFDR algorithm to extract the distributed back-scattered intensity, one can determine the position shift of the correlation peak and accurately define a temperature change within that position.^[29]

Here the monitored Rayleigh peak amplitude during annealing corresponds to an average over the entire length of the irradiated segment. The variations in the scattered amplitude are partly correlated with the change of the Retardance amplitude (Figure 4). However, even if they partly own a similar origin (e.g., nanopores formation), these two properties are not exactly representative of the same phenomenon namely dielectric constant fluctuation at the nanoscale for the Rayleigh scattering while the retardance is related to overall birefringence. The scattered light amplitude for all three fibers showed varying degrees of decline from 800 to 1000 °C, which could be attributed to the structural relaxation of the laser modification regime. Then, an important decrease of the amplitude is

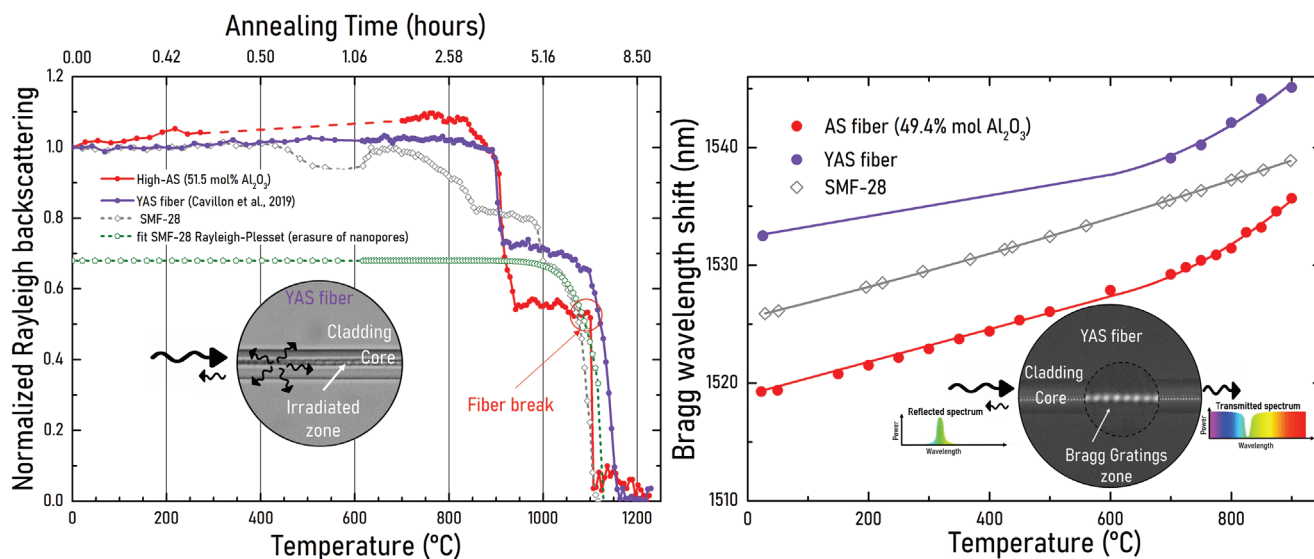


Figure 5. a) Normalized Rayleigh backscattered light from irradiated fiber segments as a function of isochronal ($\Delta t = 30$ min) temperature for sapphire-derived fiber (red), YAG-derived fiber (purple), and SMF 28 fiber (grey). Simulation of the nanopores' erasure in SMF 28 fiber using the Rayleigh–Plesset equation is added (green) and normalized to the amplitude (at 1000 °C) of the SMF 28 fiber. Experimental conditions are: Pulse energy = 0.8 μ J, $\lambda = 1030$ nm, 100 kHz, 100 μ m s⁻¹, 1000 pulses μ m⁻¹, NA = 0.6, laser polarization perpendicular to the writing direction. b) Temperature dependence of Bragg wavelength for FBGs. The fitted lines are added for each fiber as guides to the eye.

observed following the increase of the annealing temperature. In agreement with Figure 4, YAG-derived fiber shows slightly better thermal stability than the SMF-28 fiber; unfortunately, the sapphire-derived fiber sample broke around 1100 °C, so this data is not available beyond this point.

The Rayleigh scattering measurements compare well with the simulated ones (deduced from Rayleigh–Plesset equation, green curve in Figure 5a), indicating that the final observed decay could be attributed to the nanopore erasure process. Both curves start their strong decrease around the same temperature (1000 °C) and show a similar trend after.

Additionally, fiber Bragg gratings (FBGs) were inscribed in the molten core fibers and SMF-28 fiber using a point-by-point technique (see Experimental section). FBGs are a spatially periodic modulation of the refractive index inside the fiber core over a length of about a few millimeters,^[30] hence lead to a reflected light satisfying the Bragg condition and with a central wavelength of $\lambda_B = 2n_{\text{eff}}\Lambda$ with Λ being the grating period, and n_{eff} the effective modal refractive index. These optical components can then be used for temperature sensing.

Here the Bragg wavelength shift $\Delta\lambda_B(T)$ of the transmitted power was monitored as reported in Figure 5b. Both sapphire-derived and SMF-28 fibers exhibit a similar linear increase before 600 °C with an average slope around 14 pm K⁻¹. However, from 600 to 900 °C, both aluminosilicate fibers undergo a nonlinear slope increase whereas SMF-28 follows a more linear behavior. The latter is related to two main contributions: i) thermal expansion coefficient α and ii) thermo-optic coefficient $\frac{1}{n_{\text{eff}}} \frac{dn_{\text{eff}}}{dT}$. The Bragg wavelength shift $\Delta\lambda_B(T)$ follows the subsequent relationship:

$$\frac{\Delta\lambda_B}{\lambda_B} = \left(\alpha + \frac{1}{n_{\text{eff}}} \frac{dn_{\text{eff}}}{dT} \right) \Delta T \quad (1)$$

In Equation (1) the former contribution (from α) principally increases nonlinearly during the annealing process,^[31] which makes it a key factor in changing the Bragg wavelength shift trend of both sapphire-derived and YAG-derived fibers. Finally, their thermal sensitivities $\frac{\Delta\lambda_B}{\lambda_B}$ from 700 to 900 °C are found approximately equal to 32.4 pm K⁻¹ and 30.1 pm K⁻¹ respectively, which are much higher than the 17 pm K⁻¹ of SMF-28 fiber in the same temperature range.

The attractiveness and originality of this work is to choose a material approach instead of a geometrical one (see for instance in Ref. [32]) to substitute the most used sensor-based glasses, being telecom fibers. We consider “conventional” fibers with circular core/cladding geometry since microstructured optical fibers have several practical drawbacks: i) they are more expensive and complex to fabricate, ii) lack flexibility, iii) are difficult to splice with conventional splicers and with conventional fibers. Moreover, optical device laser writing such as FBGs is more complicated (needs angular positioning) than in molten core or telecom fibers. In addition, from sensing applications point of view, such microstructured fibers own a significant birefringence (due to the hole's size and shape imperfections), which makes the sensing measurements very sensitive to the polarization state and thus less reliable. Finally, the MCM fibers studied here own a much higher thermal sensitivity (30–32 pm K⁻¹) at high-temperature than all silica fibers (≈ 15 –16 pm K⁻¹^[33]).

For completeness, and while a topic of continuous study, the lifetime prediction (time/temperature couple) of these optical devices can be anticipated using accelerated ageing experiments. A master curve formalism can be employed as was recently done for nanogratings in silica glass,^[34] through a series of either isochronal or isothermal annealing experiments. Moreover, a passivation treatment can be employed

to erase the unstable part of the fabricated optical device, and consequently limiting optical response drifts (e.g., Bragg wavelength λ_B shift) over time. Following this process, in SiO_2 we predicted that a FBG will remain stable for 10 000 h and its refractive index contrast would decrease only by 7% after 10 years of operation at 800 °C and can even survive over 100 years with predictable erasure kinetic.

3. Conclusions

Aluminosilicate fibers fabricated using the MCM can be used to develop a new range of optical sensing devices in harsh environments. Using a fs laser to achieve high-intensity fields and restructuring the glass materials at the nanoscale, the photo-inscription of thermally stable optical properties inside these fibers is proven possible. Among the main results to highlight, the thermal erasure of nanogratings in a highly Al_2O_3 -containing (51.5 mol%) sapphire-derived fiber was found to overcome the performance of both conventional telecom fiber (SMF-28) and pure silica cladding using the same heat-treatment conditions. The full erasure of nanogratings was comparatively measured at ≈ 1200 °C and ≈ 1100 °C for the sapphire-derived and SMF-28 fiber or pure silica cladding, respectively. Additionally, the other MCM fabricated fibers, including YAG-derived and 42.5 mol% Al_2O_3 sapphire-derived fiber, were found to perform as good as the standard fiber. Subsequently to these findings, two types of temperature fiber sensors, based on Rayleigh backscattering and fiber Bragg grating, were fabricated in these MCM fibers. They demonstrate the ability to successfully functionalize these fibers, and exhibited enhanced thermal sensitivity (≈ 30 pm K^{-1}) compared to conventional fibers (17 pm K^{-1}) in the high temperature regime (typ. >800 °C). Consequently, we believe this technique presents an ideal large-scale platform for the next generation of harsh environment sensing devices, and further work is underway to characterize the FBGs inscribed in these fiber “families” for lifetime prediction analysis.

Table 1. Labels and compositions of the investigated optical fibers.

Label	Core center composition (molar percentage)
Sapphire-derived fiber	51.5% Al_2O_3 – 48.5% SiO_2
	42.5% Al_2O_3 – 57.5% SiO_2
SMF-28	4% GeO_2 – 96% SiO_2
YAG-derived fiber	19.5% Al_2O_3 – 8.7% Y_2O_3 – 71.8% SiO_2

4. Experimental Section

EMA and Raman Spectroscopy Studies: The investigated fibers were labeled as sapphire-derived fibers (two compositions), SMF-28 (Corning conventional single-mode fiber) and YAG-derived fiber.^[15] Table 1 reports the fiber core center compositions for each of them. The MCM was used to fabricate the sapphire- and YAG-derived fibers,^[8,35] resulting in a graded-index profile.^[36] The compound concentration profiles across the fiber core were measured by electron microprobe analysis (EMA, ZEISS SUPRA 55 VP SEM, 15 keV). The fiber segments were cleaved, mounted on a sample holder, and carbon-coated prior to the analysis. The composition profiles showed a typical parabolic profile as displayed in Figure 6a for the sapphire-derived fibers. The graded-index profile was related to the dissolution and diffusion of the cladding glass into the fluid molten core during fiber drawing.^[37]

Raman spectra of both aluminosilicate and YAG-derived fiber cores were shown in Figure 6b, along with the spectrum of pure fiber cladding (SiO_2), used as reference. The sharp peaks located ≈ 490 and 600 cm^{-1} , also called D1 and D2 defect lines, were ascribed to the breathing modes of 4- and 3-membered rings, respectively. By increasing the Al_2O_3 content, both peaks demonstrate a clear intensity decrease, which indicates that the addition of alumina causes modifications of the ring statistics in the silica glass network.^[38] The band near 800 cm^{-1} results from the motion of Si atoms in their tetrahedral oxygen cage,^[39] and the intensity of this band relatively decreases and was shifted toward lower wavenumbers when alumina content increases. This could be associated to a decrease in the number of silicon-bridging oxygen bonds. In agreement with this view, the presence of a band peaking at 890 – 900 cm^{-1} attributed to NBOHC ^[40] that was already observed in irradiated samples exposed to high radiations doses^[40,41] (γ or neutrons) and recently by fs-laser in SiO_2 .^[42]

Finally, the high-frequency bands at about 850 – 1300 cm^{-1} are usually related to the Si–O asymmetric stretching vibrations. The bands at

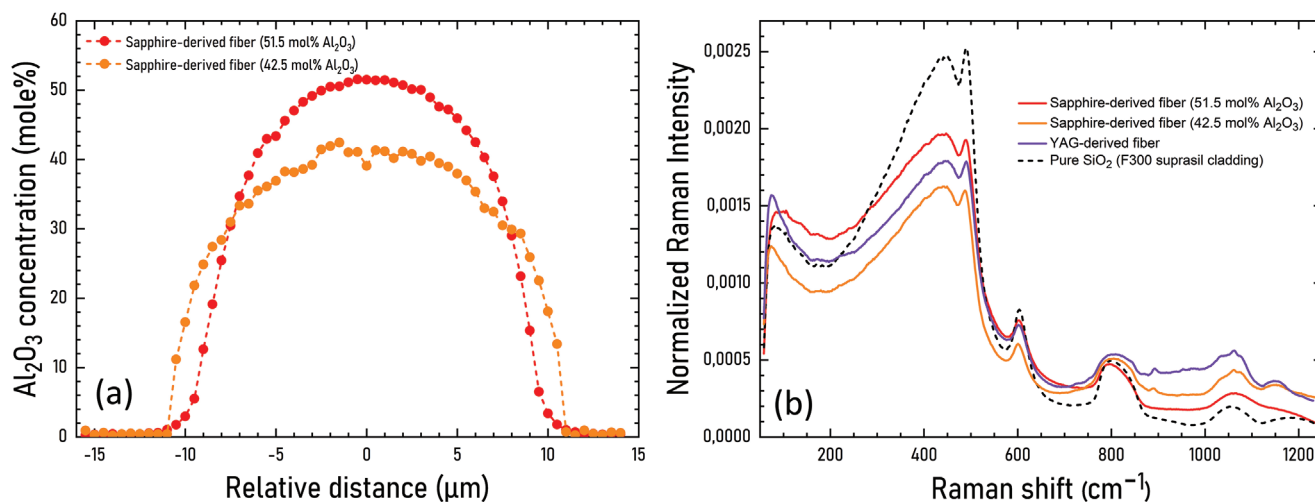


Figure 6. a) Concentration profile of two fibers core composition. b) Raman spectra of aluminosilicate fiber cores. The spectrum of the SiO_2 fiber cladding and YAG-derived fiber are also inserted for sake of comparison.

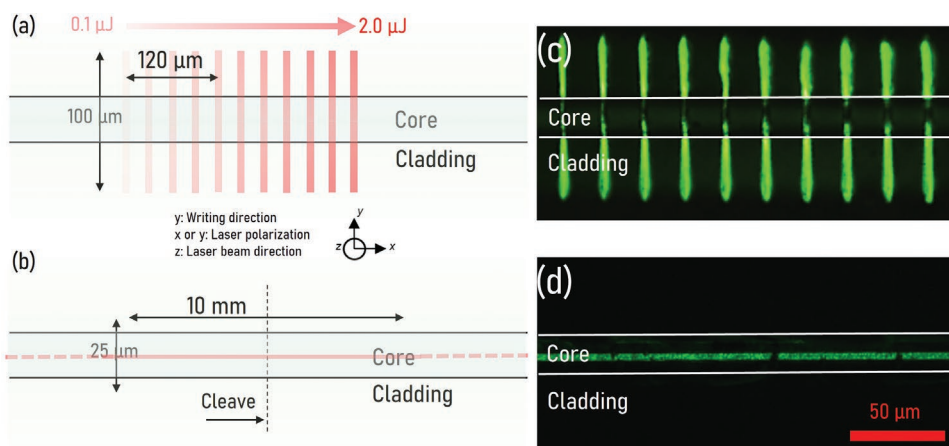


Figure 7. a) Irradiation of fs laser inside fiber core and cladding of an optical fiber at different pulse energies ($\lambda = 1030$ nm, 100 kHz, $100 \mu\text{m s}^{-1}$, 10^3 pulses μm^{-1} , NA = 0.6, pulse duration = 250 fs). b) Longitudinal (along with x) irradiation at $1.0 \mu\text{J}$ using different laser polarization conditions: parallel (\parallel , along with x) and perpendicular (\perp , along y) to the writing direction. c, d) optical microscope (bottom light illumination) image of the sapphire-derived fiber (51.5 mol% Al_2O_3) with a cross polarizer taken from (a), (b) respectively.

around $\approx 1060 \text{ cm}^{-1}$ and $\approx 1150 \text{ cm}^{-1}$ are observed in the spectra of cladding (pure SiO_2), which represents tetrahedral SiO_4 groups. In contrast, the formed interconnected Si-O-Al network^[38,43] could be found in the case of the aluminosilicates because of the high amount of Al_2O_3 . Notice there was no evidence that crystallization has occurred in the center of the fiber core and all the band shifts is similar to previously reported work, such as in Ref. [27a,44]. This was confirmed by additional EBSD analysis that did not detect any crystalline structure.

Laser Writing Experiments and Post-Irradiation Characterization: All fibers were inscribed by fs laser irradiation ($\lambda = 1030$ nm, 250 fs) following a pattern similar to a line-by-line or point-by-point FBG writing. A 5 cm long fiber segment with coating removed was taken before the irradiation and fixed on a fused silica glass slide. A borosilicate cover slip ($\approx 170 \mu\text{m}$ thin) was then placed on top of the fiber segment, and an index-matching oil (GN Nettest, $n = 1.4580$ at 25°C) was used to ensure a refractive index continuity of the setup for both optical microscope observation and irradiation. In addition, for the subsequent heat treatment, the ends of each fiber segments were fixed to Infrasil silica glass substrate by using high-temperature adhesive.

The prepared samples were positioned on a XYZ motorized translation stage, and a series of $100 \mu\text{m}$ long lines was inscribed along the x-axis with a linear laser polarization oriented either parallel (Yy configuration) or perpendicular (Yx configuration) to the writing direction. The spacing between each line is $30 \mu\text{m}$, and the pulse energy varied by steps of $0.1 \mu\text{J}$, ranging from 0.1 to $2.0 \mu\text{J}$. This is shown in Figure 7a. The laser pulse repetition rate was fixed to 100 kHz, the scanning speed to $100 \mu\text{m s}^{-1}$ and the laser beam was focused using a 0.6 NA aspheric lens. The laser parameter settings was chosen based on previous work,^[8] which was known to induce Type II permanent modifications in $\text{SiO}_2\text{-Al}_2\text{O}_3$ binary core glasses.

10 mm point per point fiber Bragg gratings (FBGs) were also written in all three fibers using a point per point direct writing technique.^[45] For the fabrication of FBGs, the acousto-optic modulator (AOM) was driven by a square wave with a given frequency smaller than the laser repetition rate (here 100 kHz), producing burst trains of fs pulses, therefore creating localized refractive index changes. FBGs can thus be written with a periodicity $\Lambda = v/f$ that depends on the ratio between the translation speed of the stage, v , and the AOM signal frequency, f . Here the AOM was fixed to 165 Hz and v to $265 \mu\text{m s}^{-1}$ resulting in a third-order grating.

To measure the optical retardance (R) induced by the fabricated nanogratings, an Olympus BX51 polarizing optical microscope equipped with a de Sénarmont compensator was used. The retardance is defined as $R = B \cdot d$, with B is the linear birefringence and d is the thickness of

the birefringent object (generally expressed in nm). The “de Sénarmont” method couples a highly precise quarter wavelength birefringent quartz or mica crystalline plate with a 180° rotating analyzer to provide retardation measurements having an accuracy that approaches one-thousandth of a wavelength. All measurements were performed at room temperature.

A complementary experiment was employed to investigate the irradiated fibers by using a scanning electron microscope (SEM, field-emission gun scanning electron microscope, ZEISS SUPRA 55 VP, 1 kV accelerating voltage). The writing geometry is sketched in Figure 7b: a single line of 10 mm length, parallel to the light propagation axis of the fiber, was written. Based on the previous experiment, the pulse energy was fixed at $1.0 \mu\text{J}$. Then, the fiber was cleaved within the irradiated zone and its cross-section was brought under the SEM. According to the laser polarization orientations, the nanopores could be found with the parallel configuration (Xx) and the nanolayers (sideways visualization of nanoplanes) with a regular spacing appeared when the polarization orientation was perpendicular to the writing direction (Xy). Finally, Figure 7c,d depict the birefringence in the sapphire-derived fiber which follow the laser inscription setup (a) and (b) respectively.

Accelerated Aging Experiments: Finally, the samples that followed the line-by-line inscription (Figure 7a) were isochronally ($\Delta t = 30$ min per temperature step) heat-treated with an incremental temperature increase (Typ. $\Delta T = 50$ K) up to 1200°C . After each annealing step, the retardance of each line was measured at room temperature after quenching the samples in air. The reported values, $R_{\text{norm}}(\Delta t, T)$, were all normalized to the initial value prior to any annealing $R(\Delta t, 20^\circ\text{C})$.

Meanwhile, the thermal stability of Rayleigh scattering was investigated at the Optic Fiber Sensors Laboratory (LCFO) of CEA France. Different fiber segments are uniformly irradiated by IR fs laser, namely SMF-28, sapphire-derived, and YAG-derived fibers. Laser parameters are chosen to produce nanogratings inside the fiber core resulting in a strong increase of the light scattering along this segment. Then, these fibers were spliced to single-mode fiber pigtails. Each sample was put inside a silica glass tube then inserted into the center of the horizontal tubular furnace. Type N thermocouple was used to monitor the temperature. During the step isochronal annealing process ($\Delta t = 30$ min per temperature step, from 600°C – 1000°C , $\Delta T = 100$ K; from 1000 – 1250°C , $\Delta T = 50$ K), Rayleigh backscattering level was measured during annealing using an OBR4600 from Luna based on OFDR technique. Coupled to an optical switch, the setup allows interrogating each fiber sequentially. Once the annealing process was completed, the OBR measurements were analyzed in post-processing to obtain the intensity of Rayleigh backscattered light propagating through of the different fiber optics.

Acknowledgements

Y.W., M.C., B.P. and M.L. thank Institut de chimie (IEA INC), Centre National de la Recherche Scientifique (Instrumentation aux limites) and, Agence Nationale de la Recherche (ANR-18-CE08-0004-01. J.B. and T.H. thank the High Energy Laser Joint Transition Office under grant N00014-17-1-2546 and the J. E. Sirrine Foundation for their financial support.

Conflict of Interest

The authors declare no conflict of interest.

Data Availability Statement

The data that support the findings of this study are available from the corresponding author upon reasonable request.

Keywords

birefringence, femtosecond lasers, fiber sensors, Rayleigh backscattering

Received: February 17, 2022

Revised: May 25, 2022

Published online: June 30, 2022

- [1] A. Rowstron, in *Adv. Photonics*, Optica Publishing Group, Zurich, Switzerland **2018**.
- [2] a) J. Canning, *Measurement* **2016**, *79*, 236; b) S. J. Mihailov, D. Grobnic, C. Hnatovsky, R. B. Walker, P. Lu, D. Coulas, H. Ding, *Sensors* **2017**, *17*, 2909.
- [3] Y. Waku, N. Nakagawa, T. Wakamoto, H. Ohtsubo, K. Shimizu, Y. Kohtoku, *J. Mater. Sci.* **1998**, *33*, 1217.
- [4] a) J. Zhang, A. Čerkauskaitė, R. Drevinskas, A. Patel, M. Beresna, P. G. Kazansky, in *Laser-based Micro- and Nanoprocessing X, Proc. SPIE*, Vol. 9736 (Eds: U. Klotzbach, K. Washio, C. B. Arnold), SPIE, Bellingham, WA **2016**, p. 97360U; b) S. J. Mihailov, *Sensors* **2012**, *12*, 1898; c) S. Musikant, *Optical Materials: An Introduction to Selection and Application*, CRC Press, Boca Raton, FL **2020**.
- [5] a) R. B. Walker, H. Ding, D. Coulas, D. Grobnic, S. J. Mihailov, M. A. Duchesne, R. W. Hughes, D. J. McCalden, R. Burchat, in *24th Int. Conf. on Optical Fibre Sensors, Proc. SPIE*, Vol. 9634, SPIE, Bellingham, WA **2015**, p. 96343X; b) F. Mezzadri, Universidade Tecnológica Federal do Paraná, **2012**.
- [6] D. Grobnic, C. W. Smelser, S. J. Mihailov, R. B. Walker, *Meas. Sci. Technol.* **2006**, *17*, 1009.
- [7] J. Ballato, P. D. Dragic, *Int. J. Appl. Glass Sci.* **2021**, *12*, 3.
- [8] J. Ballato, A. Peacock, *APL Photonics* **2018**, *3*, 120903.
- [9] Y. Shimotsuma, P. Kazansky, J. Qiu, K. Hirao, *Phys. Rev. Lett.* **2003**, *91*, 247405.
- [10] M. Lancry, B. Pommellec, J. Canning, K. Cook, J. C. Poulin, F. Brisset, *Laser Photonics Rev.* **2013**, *7*, 953.
- [11] C. Fan, B. Pommellec, M. Lancry, X. He, H. Zeng, A. Erraji-Chahid, Q. Liu, G. Chen, *Opt. Lett.* **2012**, *37*, 2955.
- [12] E. Bricchi, P. G. Kazansky, *Appl. Phys. Lett.* **2006**, *88*, 2;
- [13] T. Elsmann, A. Lorenz, N. S. Yazd, T. Habisreuther, J. Dellith, A. Schwuchow, J. Bierlich, K. Schuster, M. Rothhardt, L. Kido, H. Bartelt, *Opt. Express* **2014**, *22*, 26825.
- [14] P. Dragic, T. Hawkins, P. Foy, S. Morris, J. Ballato, *Nat. Photonics* **2012**, *6*, 627.
- [15] M. Cavillon, M. Lancry, B. Pommellec, Y. Wang, J. Canning, K. Cook, T. Hawkins, P. Dragic, J. Ballato, *J. Phys.: Photonics* **2019**, *1*, 042001.
- [16] Y. Wang, M. Cavillon, N. Ollier, B. Pommellec, M. Lancry, *Phys. Status Solidi* **2022**, *219*, 2100023.
- [17] a) M. Lancry, B. Pommellec, A. Chahid-Erraji, M. Beresna, P. Kazansky, *Opt. Mater. Express* **2011**, *1*, 711; b) R. Desmarchelier, B. Pommellec, F. Brisset, S. Mazerat, M. Lancry, *World J. Nano Sci. Eng.* **2015**, *5*, 115.
- [18] Y. Wang, S. Wei, M. R. Cicconi, Y. Tsuji, M. Shimizu, Y. Shimotsuma, K. Miura, G. D. Peng, D. R. Neuville, B. Pommellec, *J. Am. Ceram. Soc.* **2020**, *103*, 4286.
- [19] E. Bricchi, B. G. Klappauf, P. G. Kazansky, *Opt. Lett.* **2004**, *29*, 119.
- [20] J. D. Musgraves, J. Hu, L. Calvez, *Springer Handbook of Glass*, Springer, New York **2019**.
- [21] M. Nogami, K. Watanabe, Y. Ito, H. Ito, H. Nakano, *J. Am. Ceram. Soc.* **2010**, *93*, 3752.
- [22] D. Grobnic, S. J. Mihailov, J. Ballato, P. D. Dragic, *Optica* **2015**, *2*, 313.
- [23] M. Cavillon, Y. Wang, B. Pommellec, F. Brisset, M. Lancry, *Appl. Phys. A* **2020**, *126*, 876.
- [24] Y. Wang, M. Cavillon, N. Ollier, B. Pommellec, M. Lancry, *Phys. Status Solidi A* **2021**, *218*, 2100023.
- [25] B. Pommellec, M. Lancry, *Fibers* **2015**, *3*, 206.
- [26] a) J. MacDowell, G. Beall, *J. Am. Ceram. Soc.* **1969**, *52*, 17; b) S. Liu, V. Boffa, D. Yang, Z. Fan, F. Meng, Y. Yue, *J. Non-Cryst. Solids* **2018**, *492*, 77.
- [27] a) D. R. Neuville, L. Cormier, V. Montouillout, P. Florian, F. Millot, J.-C. Rifflet, D. Massiot, *Am. Mineral.* **2008**, *93*, 1721; b) R. Weber, S. Sen, R. E. Youngman, R. T. Hart, C. J. Benmore, *J. Phys. Chem. B* **2008**, *112*, 16726.
- [28] X. Bao, L. Chen, *Sensors* **2012**, *12*, 8601.
- [29] M. Wang, K. Zhao, J. Wu, Y. Li, Y. Yang, S. Huang, J. Zhao, T. Tweedle, D. Carpenter, G. Zheng, *Int. J. Extreme Manuf.* **2021**, *3*, 025401.
- [30] T. Habisreuther, T. Elsmann, Z. Pan, A. Graf, R. Willsch, M. A. Schmidt, *Appl. Therm. Eng.* **2015**, *91*, 860.
- [31] R. Brueckner, *J. Non-Cryst. Solids* **1970**, *5*, 123.
- [32] E. Schattner, S. Warren-Smith, L. V. Nguyen, D. Otten, D. Lancaster, H. Ebendorff-Heidepriem, in *2018 IEEE Sens. Proc.*, IEEE, Piscataway, NJ **2018**.
- [33] D. Su, X. Qiao, *Opt. Express* **2022**, *30*, 9156.
- [34] Y. Wang, M. Lancry, M. Cavillon, B. Pommellec, *Opt. Lett.* **2022**, *47*, 1242.
- [35] S. Morris, J. Ballato, *Am. Ceram. Soc. Bull.* **2013**, *92*, 24.
- [36] T. Elsmann, A. Lorenz, N. S. Yazd, T. Habisreuther, J. Dellith, A. Schwuchow, J. Bierlich, K. Schuster, M. Rothhardt, L. Kido, *Opt. Express* **2014**, *22*, 26825;
- [37] M. Cavillon, P. Dragic, B. Faugas, T. W. Hawkins, J. Ballato, *Materials* **2019**, *12*, 2898.
- [38] a) M. Okuno, N. Zotov, M. Schmücker, H. Schneider, *J. Non-Cryst. Solids* **2005**, *351*, 1032; b) M. F. Ando, O. Benzine, Z. Pan, J.-L. Garden, K. Wondraczek, S. Grimm, K. Schuster, L. Wondraczek, *Sci. Rep.* **2018**, *8*, 5394.
- [39] P. McMillan, *Am. Mineral.* **1984**, *69*, 622.
- [40] D. Di Francesca, A. Boukenter, S. Agnello, A. Alessi, S. Girard, M. Cannas, Y. Ouerdane, *J. Raman Spectrosc.* **2017**, *48*, 230.
- [41] M. León, L. Giacomazzi, S. Girard, N. Richard, P. Martín, L. Martín-Samos, A. Ibarra, A. Boukenter, Y. Ouerdane, *IEEE Trans. Nucl. Sci.* **2014**, *61*, 1522.
- [42] M. Royon, E. Marin, S. Girard, A. Boukenter, Y. Ouerdane, R. Stoian, *Opt. Mater. Express* **2019**, *9*, 65.
- [43] M. Busch, W. Ecke, I. Latka, D. Fischer, R. Willsch, H. Bartelt, *Meas. Sci. Technol.* **2009**, *20*, 115301.
- [44] P. F. McMillan, G. H. Wolf, B. T. Poe, *Chem. Geol.* **1992**, *96*, 351.
- [45] H. Zhang, S. M. Eaton, J. Li, A. H. Nejadmalayeri, P. R. Herman, *Opt. Express* **2007**, *15*, 4182.